

The gas turbulence in planetary nebulae: quantification and multi-D maps from long-slit, wide-spectral range echellogram. ^{*}

F. Sabbadin¹, M. Turatto², S. Benetti¹, R. Ragazzoni¹, and E. Cappellaro¹

¹ INAF - Astronomical Observatory of Padua, Vicolo dell'Osservatorio 5, I-35122 Padua, Italy

² INAF - Astrophysical Observatory of Catania, Via S. Sofia 78, I-95123 Catania, Italy

Received January 21, 2008; accepted June 17, 2008

ABSTRACT

Context. This methodological paper is part of a short series dedicated to the long-standing astronomical problem of de-projecting the bi-dimensional, apparent morphology of a three-dimensional distribution of gas.

Aims. We focus on the quantification and spatial recovery of turbulent motions in planetary nebulae (and other classes of expanding nebulae) by means of long-slit echellograms over a wide spectral range.

Methods. We introduce some basic theoretical notions, discuss the observational methodology, and develop an accurate procedure disentangling all broadening components (instrumental resolution, thermal motions, turbulence, gradient of the expansion velocity, and fine structure of hydrogen-like ions) of the velocity profile in all spatial positions of each spectral image. This allows us to extract random, non-thermal motions at unprecedented accuracy, and to map them in 1-, 2- and 3-dimensions.

Results. We discuss general and specific applications of the method. We present the solution to practical problems in the multi-dimensional turbulence-analysis of a testing-planetary nebula (NGC 7009), using the three-step procedure (spatio-kinematics, tomography, and 3-D rendering) developed at the Astronomical Observatory of Padua (Italy). In addition, we introduce an observational paradigm valid for all spectroscopic parameters in all classes of expanding nebulae.

Conclusions. Unsteady, chaotic motions at a local scale constitute a fundamental (although elusive) kinematical parameter of each planetary nebula, providing deep insights on its different shaping agents and mechanisms, and on their mutual interaction. The detailed study of turbulence, its stratification within a target and (possible) systematic variation among different sub-classes of planetary nebulae deserve long-slit, multi-position angle, wide-spectral range echellograms containing emissions at low-, medium-, and high-ionization, to be analyzed pixel-to-pixel with a straightforward and versatile methodology, extracting all the physical information (flux, kinematics, electron temperature and density, ionic and chemical abundances, etc.) stored in each frame at best.

Key words. planetary nebulae: general– ISM: kinematics and dynamics– ISM: structure

1. Introduction

The presence of circumstellar and interstellar gas in expansion is the typical signature of instability phases in stellar evolution, characterized by a large, prolonged mass-loss rate (planetary and symbiotic star nebulae, shells around Wolf-Rayet and luminous blue variable [LBV] stars), or even explosive events (nova and supernova remnants). The mass-loss of evolved stars occupies a strategic ground between stellar and interstellar physics by raising fundamental astrophysical problems (e. g., origin and structure of winds, formation and evolution of dust, synthesis of complex molecules), by playing a decisive role in the final stages of stellar evolution, and because it is crucial for the galactic enrichment in light and heavy elements.

In particular, the late evolution of low-to-intermediate mass stars ($1.0 M_{\odot} \leq M_* \leq 8.0 M_{\odot}$) is marked by the planetary nebula (PN) metamorphosis: an asymptotic giant

branch (AGB) star gently pushes out surface layers in a florilegium of forms, crosses the HR diagram, and reaches the white dwarf regime. ¹

According to current hydrodynamical and radiation-hydrodynamical simulations (Mellema 1994; Marigo et al. 2001; Villaver et al. 2002; Perinotto et al. 2004a, 2004b; Schönberner et al. 2005), the PN evolution is driven by its central star through (a) the AGB mass-loss history; and (b) the variation of ionizing flux and wind power in the post-AGB phase (without excluding the possible contribution of other factors, like magnetic fields and binarity of the central star; Soker 1998; Garcia-Segura et al. 1999; Mastrodemos & Morris 1999; Frank 1999).

At present, it is still unclear the relative importance of different shaping agents, their mutual influence, and how they affect the (global and small-scale) structure and kinematics of the ejected gas. Leaving simplistic “modern views” of PN evolution out of consideration, we remark that updated 1-D radiation-hydrodynamical evolutionary mod-

^{*} Based on observations made with European Southern Observatory (ESO) Telescopes at La Silla (program ID 65.I-0524).

Send offprint requests to: F. Sabbadin, franco.sabbadin@oapd.inaf.it

¹ The foregoing sentences are taken from Turatto et al. (2002), and Sabbadin et al. (2006), of whom the present paper is the ideal sequel.

els (Perinotto et al. 2004b; Schönberner et al. 2005) still partly fail in reproducing the positive expansion velocity gradient of the main shell (the Wilson’s law; Wilson 1950; Weedman 1968), and the gas distribution observed in a representative sample of carefully de-projected “true” PNe (Sabbadin et al. 2006 and references therein). Such model-PN vs. true-PN discrepancies suggest that the former tend to systematically overestimate the relative importance of wind interaction (as supported by a recent revision downward of mass-loss rates in PN central stars, due to clumping of the fast stellar wind; Kudritzki et al. 2006; Prinja et al. 2007).

An even deeper uncertainty surrounds the turbulence of expanding gas, a fundamental parameter measuring local, random, unsteady motions due to non-linear energy transfer. On the one hand, 2-D hydrodynamical simulations of wind interaction (Frank & Mellema 1994; Vishniac 1994; Mellema 1997; Dwarkadas & Balick 1998; Garcia-Segura et al. 1999, 2006) predict stratified turbulent motions peaking within shocked regions and/or ionization fronts characterized by the growth of Kelvin-Helmholtz, Vishniac or Rayleigh-Taylor instabilities. On the other hand, practical determinations based on high-resolution spectra (Guerrero et al. 1998; Acker et al. 2002; Gesicki et al. 2003, 2006; Gesicki & Zijlstra 2003, 2007; and Medina et al. 2006) provide a unique, average turbulence-value for each nebula, ranging from 0 km s^{-1} to 20 km s^{-1} .

We aim at quantifying and mapping turbulent motions in PNe by means of long-slit, wide spectral range, very-high spectral and spatial resolution echellograms at several position angles (PA), reduced and analyzed according to spatio-kinematical, tomographic and 3-D recovery methods developed at the Astronomical Observatory of Padua (Sabbadin et al. 2000, 2006, and references therein).

This introductory, methodological paper (a) dissects all broadening agents of a velocity profile; (b) describes an original procedure mapping turbulent motions in 1-, 2-, and 3-dimensions; (c) illustrates the solution to practical problems of turbulence-determination in a testing-PN; and (d) introduces an observational paradigm valid for all types of expanding nebulae.

In a forthcoming paper, we (i) will present multi-dimensional turbulence maps for a representative sample of PNe in different evolutionary phases; and (ii) will compare these observational results with expectations from hydrodynamical simulations and theoretical models.

2. Basic considerations

A PN consists of (large- and small-scale) interconnected sub-systems with different morphology, physical conditions, and kinematics. Each elementary volume within the radial slice of nebula selected by a spectrograph slit is characterized by

- 1) a regular expansion, and
- 2) random (i. e., thermal and turbulent) motions.

Thanks to the large stratification of the radiation and the kinematics, each ionic species generates the characteristic bowed-shaped spectral image sketched in Fig. 1.

Two useful and complementary reference lines of a spectral image (Sabbadin et al. 2000, 2004, and references therein) are:

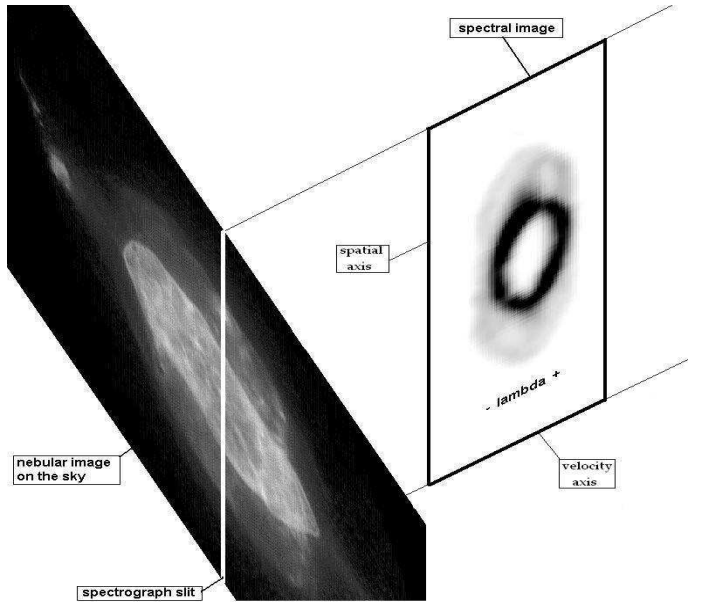


Fig. 1. Nebular projection on the sky vs. high-dispersion spectral image. The radial slice of the Saturn Nebula intercepted by a spectrograph slit crossing the central star generates a series of high-resolution spectral images; each spectral image contains kinematical and spatial information on the parent ionic species.

- the **central-star-pixel-line** (cspl), common to all PA, representing the emission of the matter projected at the apparent position of the central star, whose motion is purely radial;
- the **zero-velocity-pixel-column** (zvpc), giving the spatial intensity profile of the tangentially moving gas at the systemic radial velocity.

As illustrated in Fig. 2, the cspl of a spectral image contains the kinematical information: the intrinsic velocity profile of each nebular sub-system, convolved with a series of broadening agents (instrumental resolution, thermal motions, turbulence, and fine-structure of hydrogen-like ions), produces an observed, “Gaussianized” velocity profile, whose peak position and full-width-at-half-maximum (FWHM) of the blue- and red-shifted components give the radial velocity and the velocity spread of approaching and receding layers, respectively.

Analogously, the zvpc of a spectral image contains the spatial information: the intrinsic spatial profile of each nebular sub-system, convolved for seeing+guiding effects, produces a “Gaussianized” spatial profile, whose peak separation and FWHM give the angular distance and the thickness, respectively, of the corresponding ionic layers in the plane of the sky.

Let us consider the cspl, and focus on the FWHM of blue- and red-shifted components ($W_{total}(\text{blue})$ and $W_{total}(\text{red})$, respectively). For a typical nebular sub-system, the “Gaussianization” of the cspl is very effective, and the value of W_{total} is the sum (in quadrature) of different broadening contributions, namely:

- (A) **The gradient of the expansion velocity**, corresponding to the range in radial velocity of each emitting layer, which is usually assimilable to a Gaussian profile with W_{grad} . The value of W_{grad} changes from

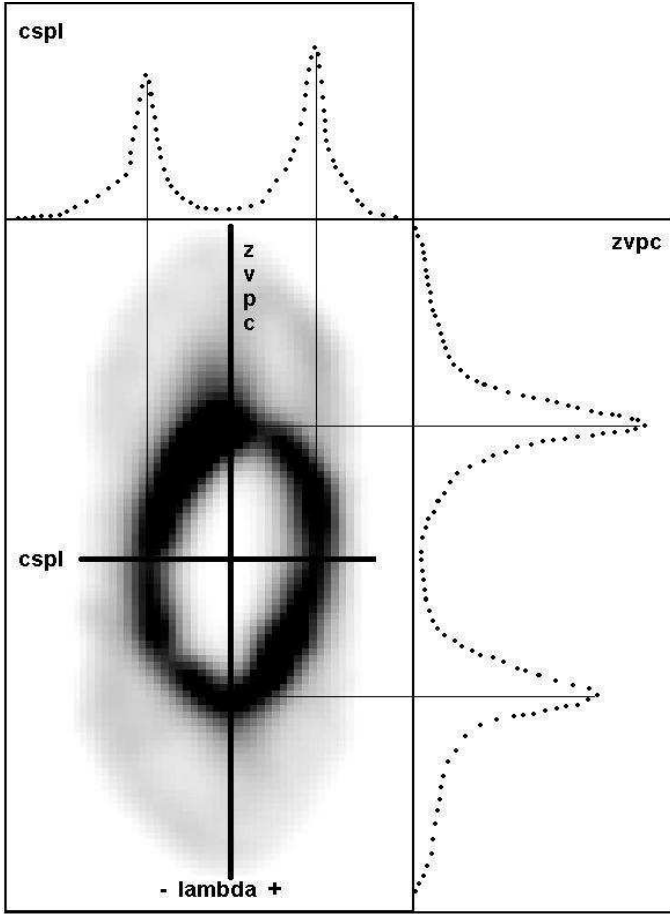


Fig. 2. Anatomy of a high-resolution spectral image, showing the location and flux distribution of both the central-star-pixel-line (cspl) and the zero-velocity-pixel-column (zvpc). More details are in the text.

one ion to another, and can be estimated from the expansion law and the spatio-kinematical reconstruction. A common case concerns an ellipsoidal PN seen at random orientations and expanding with $V_{\text{exp}}=A \times r$ ²; we have $W_{\text{grad}}=A \times \Delta r$ ², where the angular thickness Δr ² is given by the zvpc profile. Typical W_{grad} values in PN main-shells are 10 to 15 km s⁻¹ for H I, 7 to 10 km s⁻¹ for He I and He II, and 4 to 6 km s⁻¹ for ionic species of heavier elements.

- (B) **Instrumental resolution**, corresponding to a Gaussian profile with FWHM (W_{instr}), is given by the spectral resolution ($\lambda/\Delta\lambda$) of the spectrograph; a typical value of $\lambda/\Delta\lambda=50\,000$ provides $W_{\text{instr}}=6.0$ km s⁻¹.
- (C) **Thermal motions**, generating a Gaussian distribution with $W_{\text{ther}}=(8 \times k \times T_e \times \ln 2/m)^{0.5}=0.214 \times T_e^{0.5} \times m^{-0.5}$ km s⁻¹, where T_e is the local electron temperature, and m is the atomic weight of the element. Thus, for $T_e=10^4$ K, W_{ther} amounts to 21.4 km s⁻¹ for hydrogen, 10.7 km s⁻¹ for helium, 5.8 km s⁻¹ for nitrogen, and 5.4 km s⁻¹ for oxygen.
- (D) **Turbulence**, i. e., non-thermal, chaotic motions at a local scale, is characterized by W_{turb} .² Due to the intrinsically dissipative nature of turbulence (and in agree-

ment with hydrodynamical simulations; e. g., Mellema 1997; Dwarkadas & Balick 1998; Garcia-Segura et al. 1999), W_{turb} varies across the nebula, peaking in shocked layers and ionization fronts. Thus, different ionic species are affected by different turbulent motions, and, on the analogy of the radiation and the kinematics, we can introduce the concept of “stratification of the turbulence”. This means that a thorough investigation of the gas turbulence needs spectra containing emissions at high-, medium-, and low-ionization.

- (E) **The fine-structure of hydrogen-like ions**, whose levels with the same principal quantum number have small energy differences due to the spin-orbit coupling. We have performed a detailed analysis for Case B of Baker & Menzel (1938), and a l -levels population proportional to their statistical weights (Storey & Hummer 1995), obtaining $W_{fs}=7.7(\pm 0.3)$ km s⁻¹ and $5.9(\pm 0.3)$ km s⁻¹ for the seven fine-structure components of H I H α and H β , respectively (also see Clegg et al. 1999); $10.1(\pm 0.3)$ km s⁻¹ for λ 4686 Å of He II (thirteen fine-structure components); $4.2(\pm 0.3)$ km s⁻¹ for λ 6560 Å of He II (nineteen fine-structure components); and $3.0(\pm 0.3)$ km s⁻¹ for λ 5876 Å of He I (six fine-structure components). Moreover, the fine-structure profile of He II λ 4686 Å presents a weak - although showy - blue-shifted tail, and the one of He I λ 5876 Å a modest red-shifted tail. The values of W_{fs} are nearly independent on T_e for $5000 \text{ K} \leq T_e \leq 20000 \text{ K}$, and on the electron density (N_e) for $10^2 \text{ cm}^{-3} \leq N_e \leq 10^5 \text{ cm}^{-3}$.

For a typical nebular sub-system, the net turbulence-broadening in each ionic species is

$$W_{\text{turb}} = (W_{\text{total}}^2 - W_{\text{grad}}^2 - W_{\text{ther}}^2 - W_{\text{instr}}^2 - W_{fs}^2)^{0.5}. \quad (1)$$

The application of Eq. (1) to the cspl of emissions at low-, mean-, and high-ionization, combined with de-projection criteria introduced by Sabbadin et al. (2005), provides the **overall 1-D turbulence-map** of the nebula.

To be noticed: beyond the cspl, Eq. (1) applies to each pixel-line along the dispersion, thus disentangling all broadening agents of the velocity profile at all “latitudes” of a spectral image. A different-latitude-pixel-line is identified by its angular distance (d'') from the cspl; on the analogy of the latter, in the following it will be named “dlpl”.

Thus,

- I - The application of Eq. (1) to all dlpl of a spectral image allows us to map the turbulence of the parent ion within the entire de-projected nebular slice covered by a spectrograph slit (**ionic 2-D turbulence-map**);
- II - The combination of all ionic 2-D turbulence-maps at a given PA provides the **overall 2-D turbulence-map** at the corresponding PA; and
- III - By assembling overall 2-D turbulence-maps at all observed PA (for example, through the 3-D rendering procedure introduced by Ragazzoni et al. 2001), we infer the **overall 3-D turbulence-map** of the entire nebula.

Summing up, the determination of the local turbulence in 1-, 2-, and 3-dimensions passes through the constraining of

behavior for vorticity, energy dissipation and passive scalars (for a review, see Elmegreen & Scalo 2004).

² We “assume” a Gaussian probability distribution for the turbulence velocity, although some authors suggest a non-Gaussian

sinergistic broadening effects of both the instrumentation and nebular gas parameters (the latter include atomic properties, physical conditions, kinematics and ionization structure). This implies that *an adequate instrumental spectral resolution ($\lambda/\Delta\lambda \geq 50\,000$) is the “conditio sine qua non” for a quantitative study of turbulent motions in PNe, to be combined with a detailed spatio-kinematical reconstruction at high-, medium-, and low-ionization.*

In addition, large, extended nebular sub-systems (e. g., optically-thin outer shells) with a broad, flat-topped intrinsic velocity profile departing from a Gaussian distribution, provide less reliable turbulence-values than localized, compact sub-systems with a sharp intrinsic velocity profile (e. g., the main shell, condensations and knots, etc.). Last, recombination lines of H I, He I and He II are less reliable turbulence-diagnostics than collisionally-excited lines of heavier elements.

All this is illustrated in Fig. 3, showing [O III] and H I spectral images of a random seen, regularly expanding ($V_{\text{exp}} \propto r$) model-spheroid denser at the equator than at the poles, covered along the apparent major axis. We adopt three representative values of the instrumental resolution ($\lambda/\Delta\lambda=100\,000$, $50\,000$, and $25\,000$). Moreover, we assume $T_e=10^4$ K, $W_{\text{turb}}=10$ km s $^{-1}$, seeing= $1.0''$, and instrumental spatial and spectral scales of $0.20''\text{px}^{-1}$ and 1.5 km s $^{-1}$ px $^{-1}$, respectively. Different acronyms used in the current discussion (cspl, dlpl, zvp etc.) are indicated in Fig. 3, together with straight lines (a and b) containing polar and equatorial axes of the nebular slice, and their projections (a' and b') on a spectral image. According to the second de-projection rule introduced by Sabbadin et al. (2005), x-y coordinates of the nebular slice in Fig. 3 are related to x'-y' coordinates of the spectral image by:

$$y = y' \quad (2)$$

$$x = x' \times |a'' \times b''|, \quad (3)$$

where a'' and b'' are the slopes of straight lines a' and b'.

The foregoing analysis stresses a fundamental difference between imaging and spectroscopy: the former contains the bi-dimensional projection of the nebula on the sky, whose accuracy depends only on “external” factors (i. e., seeing and Airy disk for ground-based and orbiting telescopes, respectively), whereas the latter provides the pixel-to-pixel flux and velocity in different ions, and allows the nebular de-projection, whose accuracy depends on both “external” (instrumental resolution, seeing) and “intrinsic” (physical conditions, ionization, expansion, and turbulence) contributions.

The odd thing is that nebular spectra - storing much more physical information than direct imagery - are commonly integrated along the spectrograph slit, and used to infer the mean, average value of flux, electron temperature, electron density, ionic and chemical abundances, velocity, turbulence, etc. (thus, losing their precious spatial information).

3. The solution to practical problems in the multi-dimensional turbulence-analysis

Here we solve problems related to the quantification and distribution of turbulent motions in real PNe. To this end, we apply the procedure developed in Sect.

2 to a representative testing-target contained in the multi-PA, long-slit, wide spectral range, high-resolution spectroscopic survey of PNe in both hemispheres carried out with ESO NTT+EMMI (spectral range $\lambda\lambda$ 3900-8000 Å; $\lambda/\Delta\lambda=60\,000$) and Telescopio Nazionale Galileo (TNG)+SARG (spectral range $\lambda\lambda$ 4600-7900 Å; $\lambda/\Delta\lambda=114\,000$).

First, a basic observative note: our long-slit spectra cover the entire instrumental spectral range (80 and 54 orders for ESO NTT+EMMI and TNG+SARG, respectively), whereas long-slit echellograms of extended PNe are usually secured through an interference filter isolating a single order, to avoid the superposition of echelle orders. We stress that the superposition of echelle orders is unimportant for an emission-line object like a PN, the actual limit being the effective superposition of spectral images in adjacent orders. Thus, a single long-slit, wide-spectral range echellogram provides the complete spectral image in a number of emissions belonging to main ionic species, and including T_e and N_e diagnostics (Turatto et al. 2002; Benetti et al. 2003; and Sabbadin et al. 2000, 2004, 2005, 2006). This is illustrated in Fig. 4, showing the $\lambda\lambda$ 3900-8000 Å long-slit ESO NTT+EMMI rich-spectrum of NGC 3918 (PNG 294.6+04.7, Acker et al. 1992).

The order-by-order reduction procedure for long-slit, wide-spectral range echellograms uses IRAF³ and IDL packages, follows the standard method for bi-dimensional spectra (bias, CCD-flat, distortion correction, and wavelength and flux calibrations), and is fully described by Turatto et al. (2002).

We select the bright PN NGC 7009 (the Saturn Nebula, PNG 037.7-34.5, Acker et al. 1992) - observed at twelve equally-spaced PA with ESO NTT+EMMI (slit-length= $60''$) - as a test-case for the solution of practical problems in the multi-dimensional turbulence-analysis.

3.1. 1-D and 2-D turbulence-analyses of NGC 7009 close to its apparent minor axis

The Saturn Nebula is an extremely complex object, consisting of several interconnected sub-systems (including optically-thick caps and ansae, and high-excitation polar streams) with different morphology, physical conditions and kinematics. However, nebular regions projected along and close to the apparent minor axis are optically thin to the UV radiation of the central star, and their spatio-kinematical structure is relatively simple and regular (Sabbadin et al. 2004).

Spectral images of main ionic species present in NGC 7009 at PA= 124° (i. e. close to its apparent minor axis) are shown in Fig. 5, in order (left to right) of decreasing ionization potential, IP. They mark the spatio-kinematical signature in both the main shell and the outer shell of the Saturn Nebula. According to Sabbadin et al. (2004),

- (1) the former expands at $V_{\text{exp}}(\text{main shell})=4.0(\pm 0.3) \times r''$ km s $^{-1}$;

³ IRAF is distributed by the National Optical Astronomy Observatory, which is operated by the Association of Universities for Research in Astronomy, Inc., under cooperative agreement with the National Science Foundation.

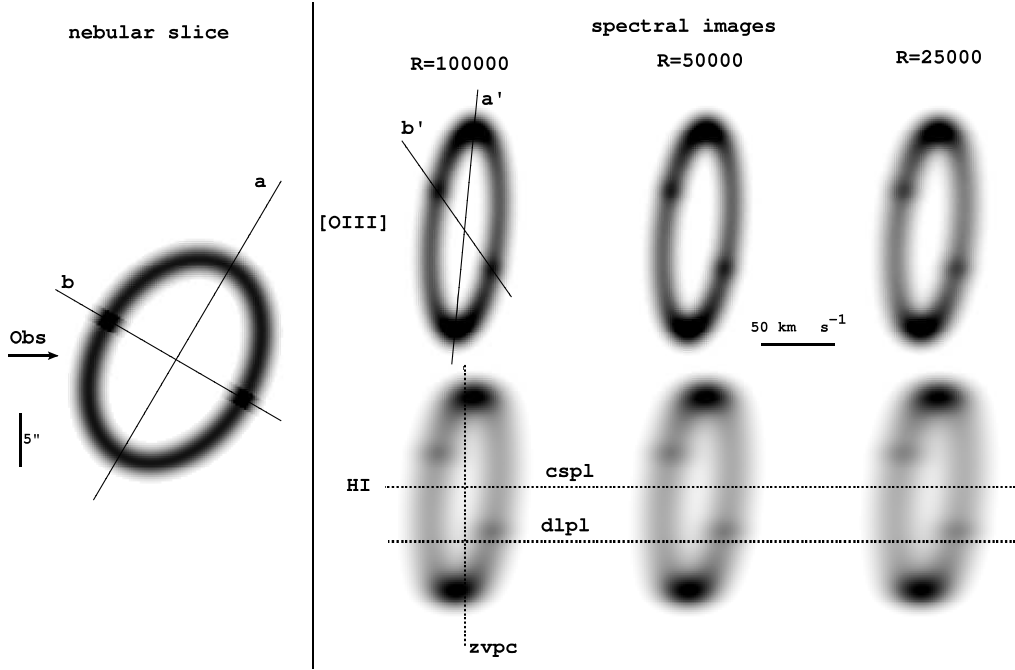


Fig. 3. A model-nebular slice and the corresponding spectral image in the collisionally-excited line $\lambda 5007 \text{ \AA}$ of [O III] and in the recombination line $\lambda 6563 \text{ \AA}$ of H I for different values of the instrumental spectral resolution. Left: model-nebular slice selected by a spectrograph slit centered on the apparent major axis of a tilted spheroid with polar diameter= $20''$, axial ratio= 1.4 , radial thickness(FWHM)= $2.0''$ and $V_{\text{exp}}(\text{km s}^{-1})=3.0 \times r''$. Right: corresponding [O III] (upper) and H I (lower) spectral images for three values of the instrumental resolution $R=\lambda/\Delta\lambda$.

- (2) the latter is slightly blue-shifted (by $3(\pm 1) \text{ km s}^{-1}$), and moves at $V_{\text{exp}}(\text{outer shell})=3.15(\pm 0.3) \times r'' \text{ km s}^{-1}$; and
- (3) de-projected tomographic maps in different ions are nearly circular rings.

Only medium- to high-excitation emissions are contained in Fig. 5, NGC 7009 being optically-thin along and close to the apparent minor axis, with a modest concentration of low-ionization species (O^0 , O^+ , S^+ , N^+ etc.).

We start with the cspl (common to all PA, and providing the 1-D turbulence-map), and then extend the analysis to the whole spectral image.

3.1.1. The 1-D turbulence-profile from the cspl

Overall cspl flux-profiles in NGC 7009 at PA= 124° are shown in Fig. 6. Besides the large broadening of H I and He II emissions, and the faint blue-shifted (red-shifted) tail characterizing the fine-structure profile of He II $\lambda 4686 \text{ \AA}$ (He I $\lambda 5876 \text{ \AA}$), Figs. 5 and 6 evidence a strong line-asymmetry due to the slightly blue-shifted outer shell.

Thus, we extract the net spectral contribution in both shells through a multi-Gaussian analysis (SPLOT routine of the IRAF package), as illustrated in Fig. 7 for [O III] $\lambda 5007 \text{ \AA}$. Such a detailed deconvolution highlights all kinematical differences between nebular sub-systems, and in particular, the broader velocity profile of the outer shell ($W_{\text{total}}(\text{blue})=21.3 \text{ km s}^{-1}$, and $W_{\text{total}}(\text{red})=20.0 \text{ km s}^{-1}$ in Fig. 7, to be compared with the corresponding value of

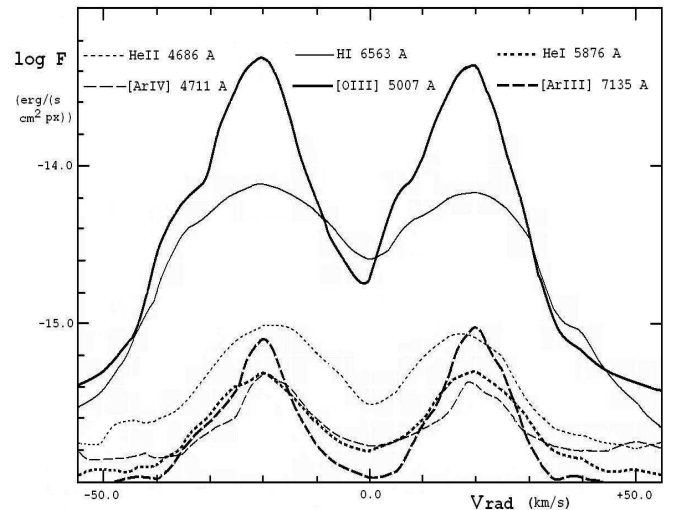


Fig. 6. The logarithmic cspl flux-profile in main emissions of NGC 7009 at PA= 124° . The observed (i. e., uncorrected for interstellar extinction) flux is in $\text{erg s}^{-1} \text{ cm}^{-2} \text{ px}^{-1}$. The X-axis is centered on the systemic velocity.

10.0 km s^{-1} for both blue- and red-shifted [O III] components of the main shell).

We analyze these two nebular sub-systems separately.

3.1.1.1. The cspl of the main shell

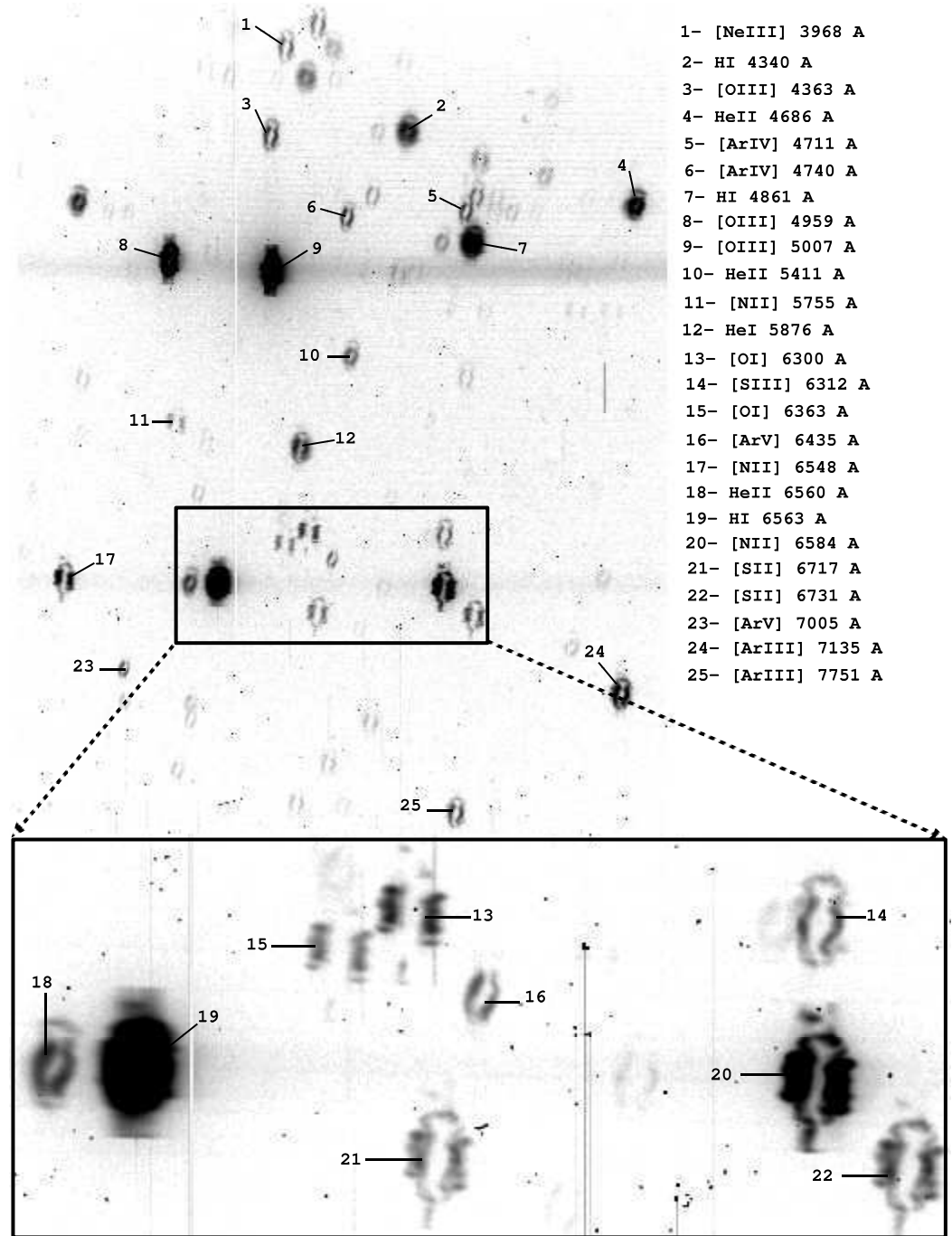


Fig. 4. The upper panel shows the main part of a $\lambda\lambda$ 3900-8000 Å, long-slit (30'') ESO NTT+EMMI spectrum (echelle order separation=4'' (blue) to 13'' (red)) of NGC 3918 at PA=101° (apparent nebular size \simeq 27''). The brightest emissions are identified. The lower part of the figure is an enlargement of the red spectral region; it enhances the richness of physical information stored in each echellogram covering 80 orders (to be compared with the single-order output provided by the usual observational procedure inserting an interference filter).

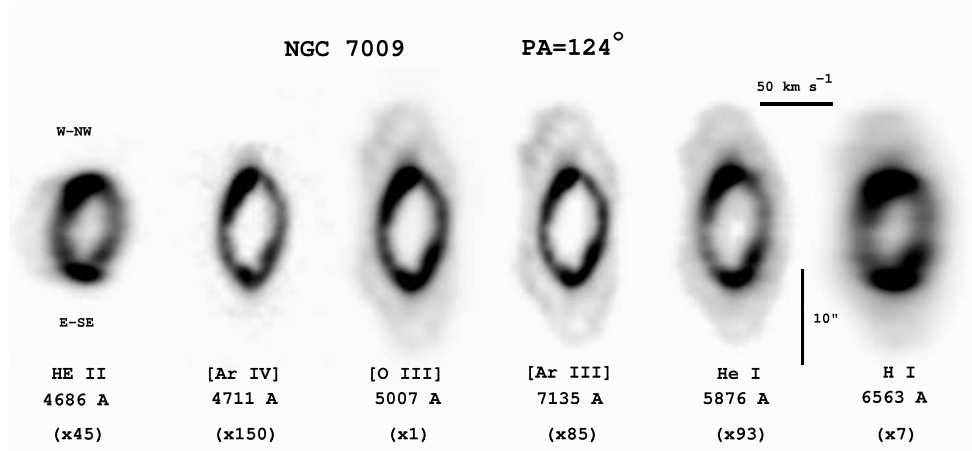


Fig. 5. The NTT+EMMI spectral image of NGC 7009 at PA=124° in six ionic species, in order - left-to-right - of decreasing IP. The slit orientation is superimposed to the left-most (He II) spectral image. The original flux is multiplied by the factor given in parenthesis, to make each emission graphically comparable with [O III] λ 5007 Å. More details are in the text.

The instrumental spectral resolution of our echellograms, estimated from night-sky lines and comparison arc spectra, amounts to $\lambda/\Delta\lambda=60\,000$ (i. e., $W_{instr}=5.0$ km s⁻¹), and is common (to within 0.5 km s⁻¹) to all ionic species. Moreover, we refer to Sect. 2 for the fine-structure broadening (W_{fs}) in different recombination lines of hydrogen-like ions. Other relevant parameters derived (or adopted) for the determination of turbulence, W_{turb} , in the cspl of the main shell of NGC 7009 at PA=124° are listed in Table 1, where:

- cols. 1 and 2 identify the emission line and the parent ion;
- cols. 3 and 4 give the W_{total} for blue- and red-shifted components of the main shell;
- col. 5 contains the adopted value of T_e (according to Hyung & Aller 1995a, 1995b; and Sabbadin et al. 2004);
- cols. 6 and 7 give the FWHM of E-SE and W-NW zvpc-peaks in the spectral image at PA=124°, providing - after correction for seeing+guiding - the radial thickness ($\Delta r''$) of each emitting layer in the main shell of NGC 7009.⁴ From $\Delta r''(cspl)\simeq\Delta r''(zvpc)$, $V_{exp}(\text{main shell})=4.0\times r''$ km s⁻¹, and $\Delta V_{exp}(\text{main shell})=W_{grad}=4\times\Delta r''$ km s⁻¹, we have

$$W_{grad} = 4\times\left[\left(\frac{\Delta r(E-SE) + \Delta r(W-NW)}{2}\right)^2 - W_{(s+g)}^2\right]^{0.5}, \quad (4)$$

⁴ In general, the value of $\Delta r(cspl)$ can be inferred from the $\Delta r(zvpc)$ trend at different PA. In the present case of NGC 7009, $\Delta r(zvpc)$ is nearly constant along and close to the apparent minor axis of the nebula (i. e., at PA=4°, 124°, 139°, 154°, and 169°).

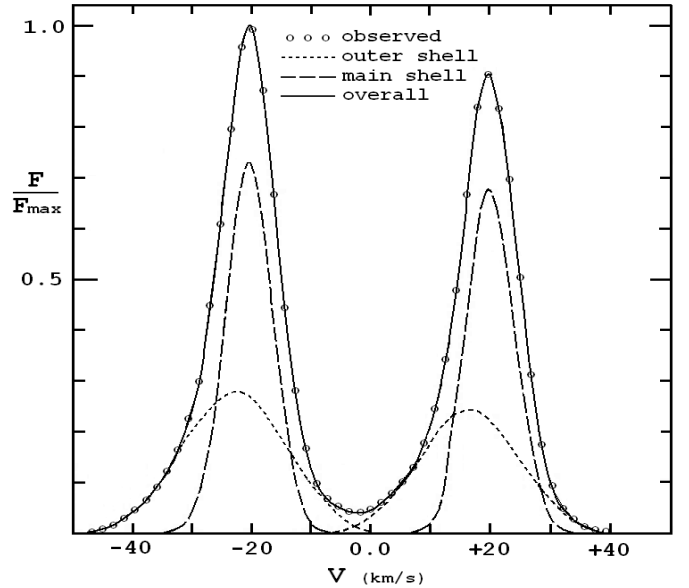


Fig. 7. Multi-Gaussian analysis of the cspl velocity-profile. The relative [O III] λ 5007 Å flux-profile observed in NGC 7009 at PA=124° (empty circles) is deconvolved in the main shell (long-dashed curve) and outer shell (short-dashed curve) contributions, and in their sum (continuous curve).

where $W_{(s+g)}$ - the seeing+guiding contribution given by the FWHM of the central star's continuum - amounts to $0.84(\pm 0.05)''$ for all emissions; and

- cols. 8 and 9 contain the resulting value of W_{turb} for blue- and red-shifted components of the cspl profile (as given by Eq. (1)). They provide the 1-D overall turbulence map in the main shell of NGC 7009 through the $V_{exp}(\text{km s}^{-1})=4.0 \times r''$ relation.

In spite of the large number of involved parameters, the estimated turbulence-accuracy in Table 1 is ± 2 to $\pm 4 \text{ km s}^{-1}$ for strong to faint collisionally-excited lines, $\pm 3 \text{ km s}^{-1}$ for He I $\lambda 5876 \text{ \AA}$, and $\pm 4 \text{ km s}^{-1}$ for H I H α and He II $\lambda 4686 \text{ \AA}$.

3.1.1.2. The cspl of the outer shell

The application of the foregoing procedure to the cspl of the outer shell in NGC 7009 at PA=124° gives unreliable turbulence values due to the huge value (and large uncertainty) of W_{grad} , which is the predominant broadening component of the velocity profile.

We consider $\lambda 5007 \text{ \AA}$ of [O III] (Figs. 5, 6, and 7). On the one hand, we obtain $W_{total}(\text{blue})=21.3(\pm 0.3) \text{ km s}^{-1}$ and $W_{total}(\text{red})=20.0(\pm 0.3) \text{ km s}^{-1}$. On the other hand, the [O III] thickness $\Delta r(\text{outer shell})$ - given by the zvpc profile corrected for seeing+guiding - amounts to $6.5(\pm 0.5)''$; it provides $W_{grad}=20.5(\pm 3.5) \text{ km s}^{-1}$ (through the $V_{exp}(\text{km s}^{-1})=3.15(\pm 0.3) \times r''$ relation valid in the outer shell).

Thus, the mere acritical, and slavish application of Eq. (1) to [O III] blue- and red-shifted components of the cspl in the outer shell furnishes $W_{turb}(\text{blue})=-4.5(\pm 9.3)^{+15.5}_{-9.3} \text{ km s}^{-1}$, and $W_{turb}(\text{red})=-8.6(\pm 6.9)^{+16.9}_{-6.9} \text{ km s}^{-1}$. Even worse results are obtained from other, fainter emissions in Figs. 5 and 6.

All this stresses the leading role of the spatio-kinematical reconstruction, whose uncertainties mark actual limits of the turbulence-analysis in PNe (to be noticed: in the absence of a spatio-kinematical recovery, the broad velocity profile in the outer shell of NGC 7009 could be ascribed to turbulent motions).

In next sections, dedicated to the 2- and 3-D mapping of turbulence, we focus on the net spectral-profile of the main shell, ignoring the outer shell (and other sub-systems) of the Saturn Nebula.

3.1.2. Ionic and overall 2-D turbulence-maps in the main shell of NGC 7009 at PA=124°

According to Sect. 2, the analysis of the velocity profile in all dlpl of a spectral image provides (through Eq. (1)) the 2-D turbulence-map of the parent ion within the entire nebular slice covered by the spectrograph slit.

The [O III] results for the main shell of NGC 7009 at PA=124° are graphically shown in Fig. 8, where each dlpl is identified by its angular distance from the cspl (d''), in units of the zvpc ionic radius $r(\text{O}^{++})=5.55''$. For practical reasons, Fig. 8 contains $W_{total}(\text{blue})$ and $W_{total}(\text{red})$ for dlpl at low-to-mean latitudes of the spectral image, whereas at high-latitudes (a) blue- and red-shifted components tend to merge, (b) spatial properties of the gas prevail on dynamical ones, and (c) the determination of W_{total} becomes problematic. Thus, for all high-latitude dlpl (i. e., $d/r(\text{O}^{++}) \geq 0.85$), we are forced to measure the “overall” FWHM of the deconvolved spectral profile, W_{over} , corresponding to

$$W_{over} = V_r(\text{red}) - V_r(\text{blue}) + \left(\frac{W_{total}(\text{blue}) + W_{total}(\text{red})}{2} \right), \quad (5)$$

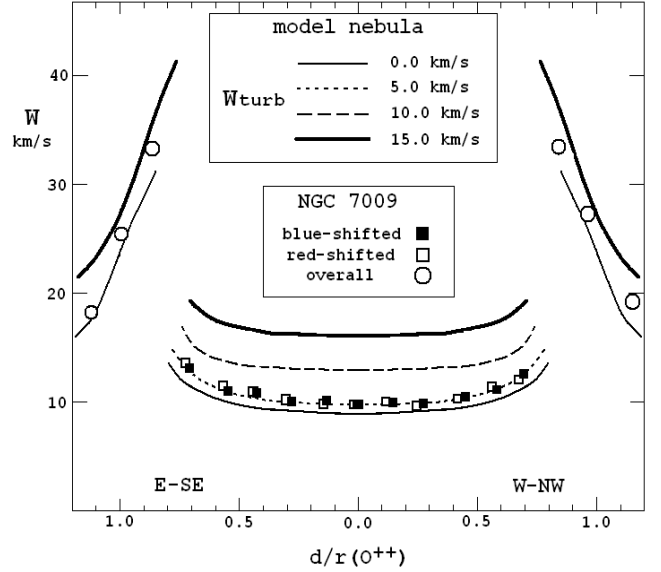


Fig. 8. Main properties of dlpl in the [O III] main shell of NGC 7009 at PA=124° (sampled along the slit with a three-pixel step, i. e., $0.84''$), superimposed to the adopted model-nebula mimicing the spatio-kinematics of the main shell in the Saturn Nebula, and characterized by different values of W_{turb} . The x-axis contains the angular distance from the cspl (d), in units of the zvpc ionic radius $r(\text{O}^{++})$. At low-to-mean latitudes (i. e., $d/r(\text{O}^{++}) \leq 0.85$) W refers to W_{total} for blue- and red-shifted components of each dlpl (squares), whereas at high-latitudes it provides the FWHM of the whole velocity-profile, i. e., W_{over} (circles).

where V_r is the radial velocity of red- and blue-shifted components in each dlpl.

For comparison, Fig. 8 also shows corresponding results for the adopted model-nebula (assuming different values for the turbulence). This circular ring-model⁵ mimics [O III] spatio-kinematical properties of the main shell of NGC 7009 at PA=124° (i. e., $r(\text{O}^{++})=5.55''$, $\Delta r(\text{O}^{++})_{corr}/r(\text{O}^{++})=0.27$,⁶ $V_{exp}=4.0 \times r'' \text{ km s}^{-1}$ and $T_e=10^4 \text{ K}$), and is observed with the same instrumentation and seeing+guiding conditions as NGC 7009.

Using the $V_{exp}(\text{main shell})=4.0 \times r'' \text{ km s}^{-1}$ relation and simple geometrical considerations, we are able to map turbulent motions within the de-projected [O III] spectral image at PA=124° (ionic 2-D turbulence-map), and the entire procedure can be repeated for other ionic species. The combination of all ionic 2-D tomographic-maps provides the overall 2-D tomographic-map of turbulence across the main shell of NGC 7009 at PA=124°. This is shown in Fig. 9, where:

- the H α contribution has been omitted (for obvious reasons);
- for He II we have used the 2-D turbulence map given by $\lambda 6560 \text{ \AA}$ (this line is fainter, but also a better turbulence diagnostic than $\lambda 4686 \text{ \AA}$);

⁵ The circular assumption applies only to untilted spectral images at PA=124°. In the other observed PA of NGC 7009, the model-nebula is a tilted ellipse (see Fig. 6 in Sabbadin et al. 2004).

⁶ Of course, $\Delta r(\text{O}^{++})_{corr}=(\Delta r(\text{O}^{++})_{obs}^2 - W_{(s+g)}^2)^{0.5}$.

Table 1. The cspl-turbulence in the main shell of NGC 7009 at PA=124°.

λ (Å)	Ion	$W_{total}(\text{blue})$ (km s ⁻¹)	$W_{total}(\text{red})$ (km s ⁻¹)	T_e (K)	$\Delta r_{(E-SE)}$ (")	$\Delta r_{(W-NW)}$ (")	$W_{turb}(\text{blue})$ (km s ⁻¹)	$W_{turb}(\text{red})$ (km s ⁻¹)
4686	He II	17.5	17.3	11 000	1.73	1.84	3.6	2.5
4711	[Ar IV]	9.9	10.1	10 500	1.55	1.65	5.5	5.8
5007	[O III]	10.0	10.0	10 000	1.68	1.72	3.4	3.4
5876	He I	14.9	14.9	10 000	1.70	1.70	6.2	6.2
6563	H I	26.1	25.5	10 000	2.42	2.38	7.6	5.2
7135	[Ar III]	8.9	9.1	10 000	1.50	1.46	4.2	4.6

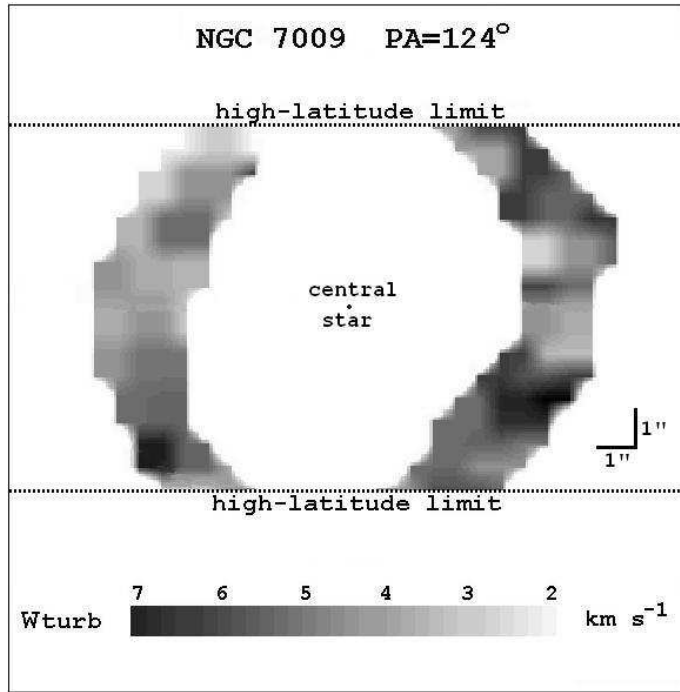


Fig. 9. The preliminary (i. e., under-sampled) tomographic turbulence-map in the main shell of NGC 7009 at PA=124°, obtained by assembling low-to-mean latitude 2-D turbulence maps in [O III], [Ar III], [Ar IV], He I and He II (λ 6560 Å). Same orientation as Fig. 5.

- the 2-D turbulence reconstruction stops at high-latitudes (since the turbulence-accuracy decreases for $d/r \geq 0.85$, due to the merging of blue- and red-shifted components); and
- pixelization is due to the discrete dlpl-sampling in each spectral image, and fuzziness to the partial superposition of turbulence-values in different ionic species.

3.2. The overall 3-D turbulence-map in the main shell of NGC 7009

The application of the whole procedure described in the foregoing section to all observed PA of NGC 7009 extracts the overall 2-D turbulence-map in twelve, equally spaced radial slices of the nebula covered by the spectrograph slit. Their assembly by means of our 3-D rendering program (Ragazzoni et al. 2001), gives the spatial distribution of

the gas-turbulence within the (almost) complete main shell (overall 3-D turbulence-map).

The preliminary (i. e., under-sampled) overall 3-D turbulence-map in the main shell of the Saturn Nebula is shown in Fig. 10 and in MOVIE N. 1 (on-line material), where:

- the W_{turb} -range is 2.0 km s⁻¹ (faintest regions) to 8.0 km s⁻¹ (brightest regions);
- the left-most (00,00) panel in Fig. 10, and the fixed image at the start of the movie represent the nebula as seen from the Earth (North is up, and East to the left); and
- the irregular, vertical, empty-band visible at (00,90) identifies high-latitude dlpl (i. e., $d/r \geq 0.85$) in original spectral images.

Although the detailed recovery and analysis of the 1-, 2-, and 3-D turbulence in NGC 7009 are beyond aims of this section (they are deferred to a dedicated paper, in preparation), we wish to underline the patchy turbulence-distribution within the main shell, and modest turbulence-values of innermost nebular regions at the highest ionization degree (i. e. He II and Ar IV emissions). In particular, the latter result

- is surprising for an extended X-ray source (Guerrero et al. 2002) like NGC 7009, whose hot and luminous powering-star ($\log T_*(K)=4.95$, $\log L_*/L_\odot = 3.70$; Sabbadin et al. 2004) is ejecting fast matter at a high - although uncertain - rate (terminal velocity $\simeq 2700$ km s⁻¹, and mass-loss in the range 3.0×10^{-10} to $1.0 \times 10^{-8} M_\odot \text{ yr}^{-1}$; Cerruti-Sola & Perinotto 1985, 1989; Bombeck et al. 1986; Hutsemekers & Surdej 1989; Tinkler & Lamers 2002);
- contrasts with hydrodynamical expectations for shocked nebular regions interacting with the hot-bubble generated by fast stellar winds (Frank & Mellema 1994; Mellema 1997; Dwarkadas & Balick 1998; Garcia-Segura et al. 1999); and
- needs confirmation by the spatio-kinematical analysis of forbidden lines at an even higher ionization degree (e. g., λ 7005 Å of [Ar V], IP=59.8 eV, and λ 3425 Å of [Ne V], IP=97.1 eV).

4. Discussion

Current theoretical models and radiation-hydrodynamical simulations of PNe predict that random, unsteady, non-

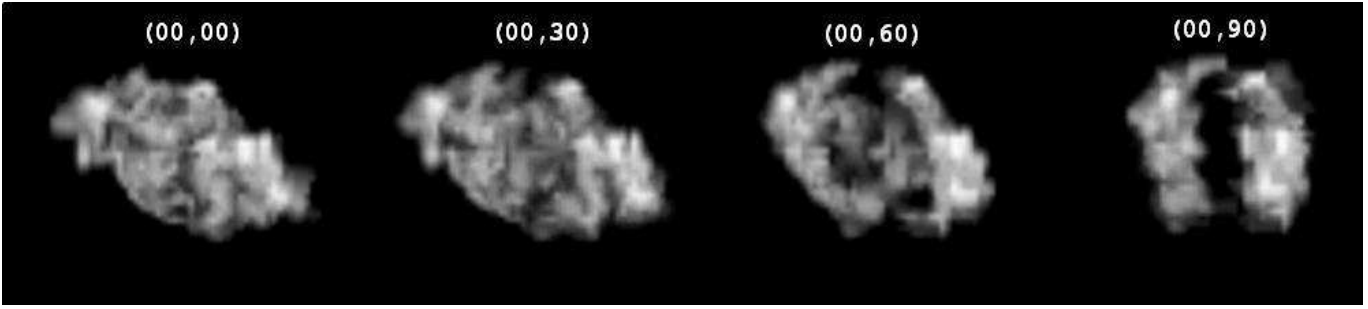


Fig. 10. Snapshots of the turbulence-structure in the main shell of NGC 7009 for a rotation around the North-South axis centered on the exciting star. The W_{turb} -range is 2.0 km s^{-1} (faintest regions) to 8.0 km s^{-1} (brightest regions). The line of sight is given by (θ, ψ) , where θ is the zenith angle, and ψ the azimuthal angle. The left-most (00,00) image corresponds to the nebula as seen from the Earth (North is up and East to the left). The complete 3-D turbulence-movie is shown in the electronic version of the paper (on-line data).

thermal motions at a local scale constitute a fundamental characteristic of the expanding gas.

Actually, our present knowledge on the turbulence-structure of real PNe is nebulous, since (1) this elusive parameter has modest kinematical effects on the complex velocity profile, and (2) practical determinations - providing a unique, average turbulence-value for each PN (Guerrero et al. 1998; Acker et al. 2002; Gesicki et al. 2003, 2006; Gesicki & Zijlstra 2003, 2007; and Medina et al. 2006) - are affected by one or more weaknesses, namely:

- (i) poor observational material (e. g., insufficient spectral resolution, very partial coverage of the nebula, limited number of emissions); and/or
- (ii) coarse data reduction (integration along the slit, assumption of spherical symmetry); and/or
- (iii) inadequate analysis (omission of some important broadening factor, absence of a spatio-kinematical reconstruction).

For these reasons, we have carried out a detailed analysis based on the three-step methodology (spatio-kinematics, tomography and 3-D recovery) developed at the Astronomical Observatory of Padua. The disentanglement of all broadening components in the velocity profile (instrumental resolution, thermal motions, turbulence, expansion gradient, and fine-structure of hydrogen-like ions) allows us the extraction of disordered non-thermal motions, and their mapping in 1-, 2-, and 3-dimensions.

Although the observed velocity-structure of a PN depends on several factors - since $W_{grad}=f(\text{ionic distribution} + \text{expansion law})$, $W_{instr}=f(\text{instrumental set-up})$, $W_{ther}=f(\text{electron temperature})$, $W_{turb}=f(\text{turbulence})$, and $W_{fs}=f(\text{atomic properties})$ -, we argue that the final turbulence-accuracy mainly depends on the reliability of its spatio-kinematical reconstruction.

Thus, *the detailed study of turbulence, of its stratification within each target and (possible) systematic variation among different sub-classes of PNe (A) is strictly connected to the general problem of de-projecting the bi-dimensional, apparent morphology of a three-dimensional mass of gas; and (B) needs (and deserves) long-slit, high-spectral resolution, multi-PA echellograms over a wide spectral range containing emissions at low-, mean-, and high-ionization, to be reduced and analyzed with a straightforward and versa-*

tive methodology extracting the whole physical information stored in each frame at best.

We underline that *the foregoing paradigm* - implying the recovery and pixel-to-pixel analysis of a large sample of emission lines in an adequate number of PA - *should be extended to all observational parameters (e. g., flux, electron temperature, electron density, ionic and chemical abundances, etc.), due to the spatio-kinematical florilegium exhibited by PNe* (Turatto et al. 2002; Benetti et al. 2003; Sabbadin et al. 2000, 2004, 2005, 2006).

We end pointing out that the methodology developed here for PNe actually applies to all types of expanding nebulae (including nova and supernova remnants, shells around Population I Wolf-Rayet stars, nebulae ejected by symbiotic stars, bubbles surrounding early spectral-type main sequence stars, etc.) covered at adequate “relative spatial” and “relative spectral” resolutions.

5. Conclusions

So far, the quantification of stratified turbulent motions in the ionized gas of PNe - as predicted by hydrodynamical simulations and theoretical models - escaped a direct verification because of its strict connection with the general, long-standing astronomical problem of de-projecting the bi-dimensional, apparent morphology of a three-dimensional mass of gas. The solution is now approached by spatio-kinematical, tomographic, and 3-D rendering analyses applied to long-slit, multi-PA, high-resolution echellograms over a wide spectral range.

We develop an accurate procedure disentangling all broadening components (instrumental resolution, thermal motions, turbulence, expansion gradient, and fine structure of hydrogen-like ions) of the velocity profile. This overcomes main weaknesses affecting previous determinations, and allows us to quantify and map in 1-, 2-, and 3-dimensions the gas-turbulence in PNe.

The multi-dimensional turbulence-analysis - soon applied to a representative sample of targets in different evolutionary phases, and combined with expectations from updated radiation-hydrodynamical simulations - will provide new, deep insights on different shaping agents of PNe (ionization, wind interaction, magnetic fields, binarity of the central star, etc.), and on their mutual interaction.

Last, we emphasize all advantages - and encourage the adoption - of long-slit echellograms covering the entire in-

strumental spectral range, since the usual insertion of an interference filter isolating a single echelle order proves superfluous and strongly limitative in most cases... it is like driving a Ferrari with the hand-brake applied.

Acknowledgements. This paper is dedicated to the memory of Prof. Mario Perinotto, an expert and generous colleague, an example of intellectual honesty, and, mainly, a dear friend... ciao, Mario.

This work was supported by grant no. 2006022731 of the PRIN of Italian Ministry of University and Science Research.

References

- Acker, A., Gesicki, K., Grosdidier, Y., & Durand, S. 2002, *A&A*, 384, 620
- Acker, A., Ochsenbein, F., Stenholm, B., et al. 1992, *Strasbourg-ESO Catalogue of Galactic Planetary Nebulae*, ESO, Garching
- Baker, J. G., & Menzel, D. H. 1938, *ApJ*, 88, 52
- Benetti, S., Cappellaro, E., Ragazzoni, R., et al. 2003, *A&A*, 400, 161
- Bombeck, G., Köppen, J., & Bastian, U. 1986, in *New Insights in Astrophysics (ESA SP-263)*, p. 287
- Cerruti-Sola, M., & Perinotto, M. 1985, *ApJ*, 291, 247
- Cerruti-Sola, M., & Perinotto, M. 1989, *ApJ*, 345, 339
- Clegg, R. E. S., Miller, S., Storey, P. J., & Kisielius, R. 1999, *A&AS*, 135, 359
- Dwarkadas, V. V., & Balick, B. 1998, *ApJ*, 497, 267
- Elmegreen, B. G., & Scalo, J. 2004, *ARA&A*, 42, 211
- Frank, A. 1999, *NewAR*, 43, 31
- Frank, A., & Mellema, G. 1994, *ApJ*, 430, 800
- Garcia-Segura, G., Langer, N., Rozyczka, M., & Franco, J. 1999, *ApJ*, 517, 767
- Garcia-Segura, G., Lopez, J. A., Steffen, W., et al. 2006, *ApJ*, 646, 61
- Gesicki, F., Acker, A., & Zijlstra, A. A. 2003, *A&A*, 400, 957
- Gesicki, F., & Zijlstra, A. A. 2003, *MNRAS*, 338, 347
- Gesicki, F., & Zijlstra, A. A. 2007, *A&A*, 467, L29
- Gesicki, K., Zijlstra, A. A., Acker, A., et al. 2006, *A&A*, 451, 925
- Guerrero, M. A., Gruendl, R. A., & Chu, Y. -H. 2002, *A&A*, 387, L1
- Guerrero, M. A., Villaver, E., & Manchado, A. 1998, *ApJ*, 507, 889
- Hutsemekers, D., & Surdej, J. 1989, *A&A*, 219, 237
- Hyung, S., & Aller, L. H. 1995a, *MNRAS*, 273, 958
- Hyung, S., & Aller, L. H. 1995b, *MNRAS*, 273, 973
- Kudritzki, R. P., Urbaneja, M. A., & Puls, J. 2006, in Barlow, M. J., & Mendez, R. H., eds, *IAU Symp. 234, Planetary Nebulae in Our Galaxy and Beyond*, Cambridge Univ. Press, Cambridge, p. 119
- Marigo, P., Girardi, L., Groenewegen, M. A. T., & Weiss, A. 2001, *A&A*, 378, 958
- Mastrodemos, N., & Morris, M. 1999, *ApJ*, 523, 357
- Medina, S., Peña, M., Morisset, C., & Stasinska, G. 2006, *RMxAA*, 42, 127
- Mellema, G. 1994, *A&A*, 290, 915
- Mellema, G. 1997, *A&A*, 321, L29
- Perinotto, M., Patriarchi, P., Balick, B., & Corradi, R. L. M. 2004a, *A&A*, 422, 963
- Perinotto, M., Schönberner, D., Steffen, M., & Calonaci, C. 2004b, *A&A*, 414, 993
- Prinja, R. K., Hodges, S. E., Massa, D. L., et al. 2007, *MNRAS*, 382, 299
- Ragazzoni, R., Cappellaro, E., Benetti, S., et al. 2001, *A&A*, 369, 1088
- Sabbadin, F., Benetti, S., Cappellaro, E., et al. 2005, *A&A*, 436, 549
- Sabbadin, F., Cappellaro, E., Benetti, S., et al. 2000, *A&A*, 355, 688
- Sabbadin, F., Turatto, M., Cappellaro, E., et al. 2004, *A&A*, 416, 955
- Sabbadin, F., Turatto, M., Ragazzoni, R., et al. 2006, *A&A*, 451, 937
- Schönberner, D., Jacob, R., Steffen, M., et al. 2005, *A&A*, 441, 573
- Soker, N. 1998, *ApJ*, 496, 833
- Storey, P. J. & Hummer, D. G. 1995, *MNRAS*, 272, 41
- Tinkler, C. M., & Lamers, H. J. G. L. M. 2002, *A&A*, 384, 987
- Turatto, M., Cappellaro, E., Ragazzoni, R., et al. 2002, *A&A*, 384, 1062
- Villaver, E., Manchado, A., & Garcia-Segura, G. 2002, *ApJ*, 581, 1204
- Vishniac, E. T. 1994, *ApJ*, 428, 186
- Weedman, D. W. 1968, *ApJ*, 153, 49
- Wilson, O. C. 1950, *ApJ*, 111, 279

List of Objects

‘NGC 3918’ on page 5